

# An infrared probe of the insulator-to-metal transition in $\text{Ga}_{1-x}\text{Mn}_x\text{As}$ and $\text{Ga}_{1-x}\text{Be}_x\text{As}$

B. C. Chapler,<sup>1,\*</sup> R. C. Myers,<sup>2</sup> S. Mack,<sup>3</sup> A. Frenzel,<sup>1</sup> B. C. Pursley,<sup>1</sup> K. S. Burch,<sup>4</sup>  
E. J. Singley,<sup>5</sup> A. M. Dattelbaum,<sup>6</sup> N. Samarth,<sup>7</sup> D. D. Awschalom,<sup>3</sup> and D. N. Basov<sup>1</sup>

<sup>1</sup>*Physics Department, University of California-San Diego, La Jolla, California 92093, USA*

<sup>2</sup>*Department of Materials Science and Engineering,  
Ohio State University, Columbus, Ohio 43210, USA*

<sup>3</sup>*Center for Spintronics and Quantum Computation,  
University of California-Santa Barbara, California 93106, USA*

<sup>4</sup>*Department of Physics & Institute for Optical Sciences,  
University of Toronto, Toronto, Ontario, Canada M5S 1A7*

<sup>5</sup>*Department of Physics, California State University-East Bay, Hayward, California 94542, USA*

<sup>6</sup>*Los Alamos National Laboratory, Los Alamos, New Mexico 87545, USA*

<sup>7</sup>*Department of Physics, The Pennsylvania State University, University Park, Pennsylvania 16802, USA*

(Dated: April 27, 2022)

We report infrared studies of the insulator-to-metal transition (IMT) in GaAs doped with either magnetic (Mn) or non-magnetic acceptors (Be). We observe a resonance with a natural assignment to impurity states in the insulating regime of  $\text{Ga}_{1-x}\text{Mn}_x\text{As}$ , which persists across the IMT to the highest doping (16%). Beyond the IMT boundary, behavior combining insulating and metallic trends also persists to the highest Mn doping. Be doped samples however, display conventional metallicity just above the critical IMT concentration, with features indicative of transport within the host valence band.

The insulator-to-metal transition (IMT) becomes exceptionally complex when magnetism is involved, as proven in materials such as mixed-valence manganites, rare-earth chalcogenides, and Mn-doped III-V compounds [1, 2]. In all these systems, the electronic and magnetic properties are typically interconnected, creating an enticing challenge to understand how magnetism affects the IMT physics. A promising route to isolate differences attributable to the presence of magnetism on the IMT physics is to investigate either magnetic or non-magnetic dopants in the same host. *p*-doped GaAs is well suited for the task since metallicity in this material can be initiated by non-magnetic (Zn, Be, C) and magnetic (Mn) acceptors. Infrared (IR) experiments reported here for  $\text{Ga}_{1-x}\text{Be}_x\text{As}$  and  $\text{Ga}_{1-x}\text{Mn}_x\text{As}$  monitor the charge dynamics and electronic structure in the course of the IMT. Our results establish that the onset

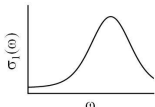
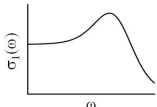
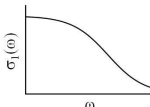
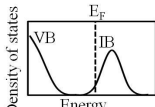
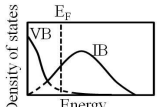
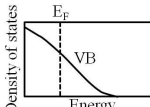
	<b>Insulator</b>	<b>IB conduction</b>	<b>Genuine metal</b>
$d\rho/dT$	$> 0$	mixed	$< 0$
Be (%)	0.0038	0.0095	0.032, 0.9
Mn (%)	0.5, 0.75	1.5 – 16	NA
Conductivity (schematic)			
Band structure (schematic)			

TABLE I: Summary of the three transport regimes uncovered for  $p$ -doped GaAs. Conductivity schematics in the insulating and impurity band conduction regimes highlight the resonance associated with valence band to impurity band transitions. This is contrasted by the conductivity schematic in the genuinely metallic regime that highlights the Drude response due to free-carriers. We only list Mn and Be dopings reported in this study.

of conduction in magnetically doped GaAs is distinct from genuine metallic behavior due to extended states in the host valence band (VB), as seen in moderately doped  $\text{Ga}_{1-x}\text{Be}_x\text{As}$ . Moreover, we observe a co-existence of “metallic” and “insulating” trends over a broad range of Mn concentrations (1-16%), underscoring the unconventional nature of Mn-doped GaAs beyond the IMT boundary.

The  $\text{Ga}_{1-x}\text{Mn}_x\text{As}$  samples were prepared using a non-rotated, low-temperature, molecular-beam-epitaxy (MBE) technique, which has been shown to minimize the formation of compensating defects [3, 4]. Several samples were also subjected to post-growth annealing in attempt to further reduce/eliminate defects. The IMT in  $\text{Ga}_{1-x}\text{Be}_x\text{As}$  occurs at much lower dopant concentrations due to the much lower acceptor level ( $E_{\text{Be}}=28$  meV,  $E_{\text{Mn}}=112$  meV [5]), thus samples near the  $\text{Ga}_{1-x}\text{Be}_x\text{As}$  IMT were grown using conventional equilibrium MBE. Importantly, the most metallic  $\text{Ga}_{1-x}\text{Be}_x\text{As}$  sample,  $\text{Ga}_{0.991}\text{Be}_{0.009}\text{As}$ , was grown under the same non-rotated, low-temperature conditions as the  $\text{Ga}_{1-x}\text{Mn}_x\text{As}$  samples. We can therefore expect nominally similar levels of disorder and charge density as that of  $\text{Ga}_{1-x}\text{Mn}_x\text{As}$  samples with  $x\sim 0.01$ . Details on sample growth can be found in the supplementary material.

Through a combination of transmission and ellipsometric measurements, we have probed the optical properties of the samples over a broad range of frequencies, spanning  $\sim 40\text{--}40,000$   $\text{cm}^{-1}$  (experimental details can be found in the supplemental material). Here we primarily focus on the real (or dissipative) part of the optical conductivity ( $\sigma_1(\omega)$ ) from THz to just below the GaAs band gap energy ( $\sim 40\text{--}10,000$   $\text{cm}^{-1}$ ). Through this probe, signatures

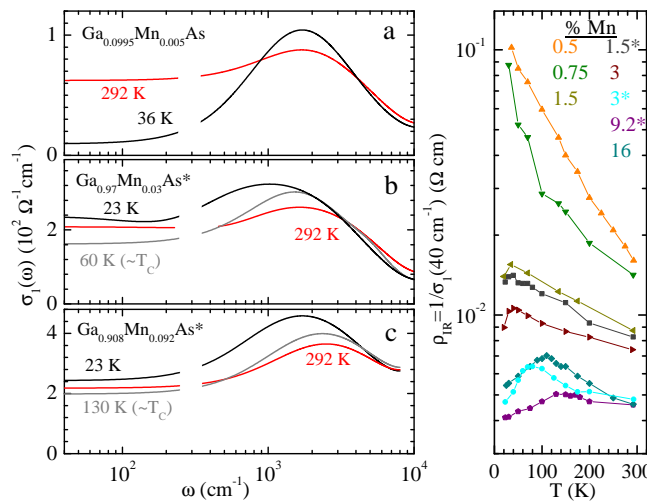


FIG. 1: Characteristic spectra of the Mn-doped samples in the insulating (a) and IB conduction (b and c) regimes are exemplified by the  $\text{Ga}_{0.995}\text{Mn}_{0.005}\text{As}$ ,  $\text{Ga}_{0.97}\text{Mn}_{0.03}\text{As}^*$ ,  $\text{Ga}_{0.908}\text{Mn}_{0.092}\text{As}^*$  samples, respectively. The break in the spectra is due to a phonon in GaAs which does not allow  $\sigma_1(\omega)$  to be extracted over this region. d) The temperature dependence of  $\rho_{\text{IR}}$  for all Mn-doped samples in the study.

of three distinct electronic transport regimes in  $p$ -doped GaAs are revealed (see Table I): a regime of insulating behavior; a regime of genuine metallic behavior (i.e. no signs of thermal activation) due to extended states in a partially unoccupied VB; and an unusual intermediate regime of conduction, exhibiting elements of both insulating and metallic transport. We refer to this latter regime as impurity band (IB) conduction, with this term used to describe the persistence of a resonance associated with VB to IB transitions beyond the onset of conductivity.

We begin by discussing the insulating regime of  $\text{Ga}_{1-x}\text{Mn}_x\text{As}$ . Fig. 1a depicts the spectra for a paramagnetic  $\text{Ga}_{0.995}\text{Mn}_{0.005}\text{As}$  sample. The dominant feature of these data is a broad mid-IR resonance, with peak frequency ( $\omega_0$ ) near  $1700\text{ cm}^{-1}$ . Room-temperature data show substantial spectral weight at far-IR frequencies (Fig. 1a). However, far-IR weight is transferred to the mid-IR resonance as the sample is cooled, and “freezes out” at low temperature. Elimination of far-IR spectral weight unambiguously reveals the thermally activated nature of the electronic transport in this dilute regime. In Fig. 1d, we plot the temperature dependence of the “infrared resistivity” ( $\rho_{\text{IR}}=1/\sigma_1(40\text{ cm}^{-1})$ ). The data in dilute Mn-doped samples ( $x=0.005, 0.0075$ ) show the systematic increase in  $\rho_{\text{IR}}$  expected in the case of thermally activated transport, in support of the conclusion of variable-range hopping inferred from direct resistivity measurements[6]. The existence of a narrow impurity band is not in dispute in dilutely doped insulating samples [7, 8], thus the observed mid-IR resonance in the vicinity of  $E_{\text{Mn}}$  in insulating samples can be naturally assigned to VB to IB transitions. We note although this is the first detailed report of a mid-IR resonance

in the insulating state, numerous probes report evidence of an IB in moderately doped  $\text{Ga}_{1-x}\text{Mn}_x\text{As}$ [9–17].

Fig. 1b and c show the spectra of the ferromagnetic  $\text{Ga}_{0.97}\text{Mn}_{0.03}\text{As}^*$  and  $\text{Ga}_{0.908}\text{Mn}_{0.092}\text{As}^*$  samples (\* denotes annealed), the highest conducting  $\text{Ga}_{1-x}\text{Mn}_x\text{As}$  samples in this study. The spectra of both of these samples are characteristic of the IB conduction regime. The dominant feature of the spectra is a mid-IR resonance, similar in shape and  $\omega_0$  to the insulating sample. These samples additionally show a finite  $\sigma_{\text{DC}}$  in the limit of  $\omega$ ,  $T \rightarrow 0$ : a condition often associated with the onset of metallicity. Nevertheless, a substantial fraction of the far-IR spectral weight still reveals activated behavior. Specifically, as the temperature is lowered from 300 K to near  $T_C$ , the far-IR spectral weight is suppressed and transferred to the mid-IR resonance, similar to data in Fig. 1.

The onset of ferromagnetism radically alters the temperature dependence of  $\sigma_1(\omega)$ . Below  $T_C$ , we observe the reversal of the activated character (black spectra in the panels b and c), as the far-IR spectral weight, as well as the mid-IR resonance are enhanced. Earlier data have established a correlation between the enhancement of the spectral weight and the development of the magnetization [10]. Such enhancement serves as an unmistakable signature of the deep bond between magnetism and carrier dynamics in this class of carrier-mediated ferromagnets and other magnetic materials[1, 18–20]. Comparison with dilute samples show the  $\rho_{\text{IR}}$  data still display (weakly) activated transport above  $T_C$ . Peaks in  $\rho_{\text{IR}}$  near  $T_C$  mark the reversal of activated trends.

Our data show the onset of conduction in  $\text{Ga}_{1-x}\text{Mn}_x\text{As}$  occurs at a doping level  $0.0075 < x \leq 0.015$ , in excellent agreement with the Mott-criterion ( $p_c^{1/3} = 2.78a_H$ , where  $p_c$  is the critical acceptor concentration and  $a_H$  is the effective Bohr radius of acceptor holes), corresponding to  $x = 0.0109$  for  $\text{Ga}_{1-x}\text{Mn}_x\text{As}$  (assuming 1 hole/Mn and no compensation) [5]. This agreement attests to a low degree of compensation in our samples, at least at doping regimes below a few atomic percent. We further note the IB conduction regime persists over an order of magnitude in dopant concentration, corresponding to at least  $x = 0.015$ – $0.16$  in  $\text{Ga}_{1-x}\text{Mn}_x\text{As}$ , as well as in heavily doped annealed samples ( $\text{Ga}_{0.908}\text{Mn}_{0.092}\text{As}^*$ ). No Mn-doped samples in this study were found to exhibit genuinely metallic behavior, which we report and describe below for  $\text{Ga}_{1-x}\text{Be}_x\text{As}$ .

Data in Fig. 2 display the IMT in  $\text{Ga}_{1-x}\text{Be}_x\text{As}$ . The  $x = 3.8 \times 10^{-5}$  and  $x = 9.5 \times 10^{-5}$  Be-doped samples (pink and grey curves in Fig. 2) reveal significant low-frequency conductivity at room temperature. However, the conductivity of the  $x = 3.8 \times 10^{-5}$  Be-doped sample is frozen out at low-temperatures, analogous to the insulating  $\text{Ga}_{1-x}\text{Mn}_x\text{As}$  samples. Also similar to  $\text{Ga}_{1-x}\text{Mn}_x\text{As}$ , both  $x = 3.8 \times 10^{-5}$  and  $x = 9.5 \times 10^{-5}$  Be-doped samples show a resonance centered in the vicinity of the  $E_{\text{Be}}$ . Such a feature near the acceptor level reinforces a VB to dopant-induced IB interpretation in both Mn- and Be-doped GaAs. The  $\rho_{\text{IR}}$  data for the  $x = 9.5 \times 10^{-5}$  sample appear to show a finite

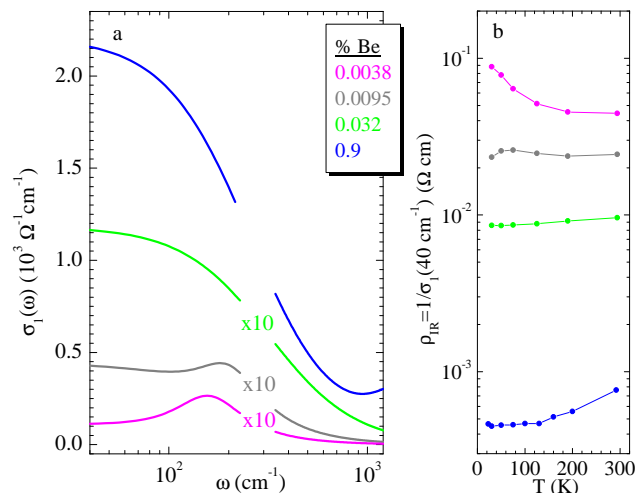


FIG. 2: a) Low temperature ( $\sim 25$  K) spectra for the  $\text{Ga}_{1-x}\text{Be}_x\text{As}$  samples. All spectra but that for the  $x=0.009$  sample are multiplied by 10 to show on the same scale. b) Temperature dependence of  $\rho_{\text{IR}}$  for all Be-doped samples.

$\sigma_{\text{DC}}$  in the limit of  $\omega, T \rightarrow 0$ , implying this sample may be past the onset of conduction. Thus an intermediate IB conduction regime could be a generic feature of  $p$ -doped GaAs (and potentially many other doped semiconductors) near the IMT [21, 22].

Moving to the  $x=3.2 \times 10^{-4}$  and  $x=0.009$  Be-doped samples (light-green and blue curves in Fig. 2), we see spectra qualitatively different from those observed in samples either in the insulating or IB conduction regimes. Here conductivity data are dominated by a pronounced Drude peak (Lorentzian centered at  $\omega=0$ ), characteristic of delocalized carriers in a metal. Insights into the nature of the metallic state in  $\text{Ga}_{1-x}\text{Be}_x\text{As}$  is revealed by applying the partial sum rule to the conductivity:

$$\int_0^{\omega_c} \sigma_1(\omega) d\omega = \frac{\pi p e^2}{2m_{\text{opt}}}. \quad (1)$$

This analysis yields the effective optical mass ( $m_{\text{opt}}$ ) provided the carrier density  $p$  is known. Using an integration cut-off of  $\omega_c=6450 \text{ cm}^{-1}$  [23], we obtain  $m_{\text{opt}} = 0.28m_e$  and  $0.29m_e$  ( $m_e$  is the electron mass) for the  $x=3.2 \times 10^{-4}$  and  $x=0.009$  Be-doped samples, respectively. The extracted  $m_{\text{opt}}$  is in excellent agreement with calculations of the IR spectra of metallic  $p$ -doped GaAs with a partially unoccupied VB, which place  $m_{\text{opt}}$  between  $0.25m_e$  and  $0.29m_e$  [24]. These results, along with the metallic temperature dependence (green and blue curves in Fig. 2b), give strong evidence of transport due to light quasiparticles in a partially unoccupied VB. Note, the Mott-criterion for Be-doped GaAs predicts a critical dopant concentration of  $x=2.7 \times 10^{-4}$  [5]. Thus our data indicate genuinely metallic behavior is

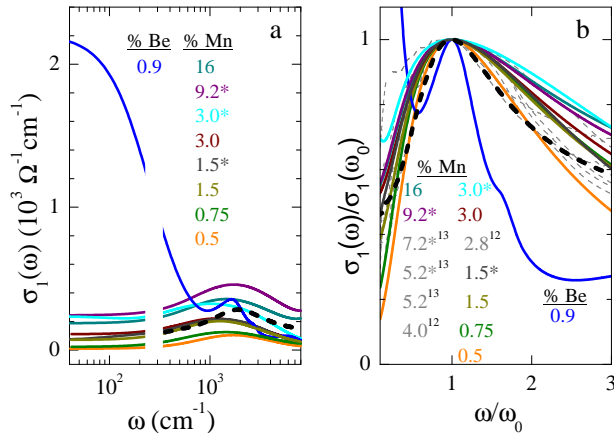


FIG. 3: a) Direct comparison of the conductivity spectra displayed for the lowest temperatures measured (20-36 K) of the  $x=0.009$  Be-doped film and all Mn-doped films studied. b) The mid-IR resonance in the two classes of materials is directly compared by normalizing spectra by the peak in  $\sigma_1(\omega)$  at  $\omega_0$  along the  $y$ -axis, and by  $\omega_0$  along the  $x$ -axis. Also shown in both panels is calculated  $\sigma_1(\omega)$  according to the quantum defect method (black dashed) [12]. Additional  $\text{Ga}_{1-x}\text{Mn}_x\text{As}$  data are reported from Burch *et al.*[11] and Singley *et al.*[10].

achieved even for a 20% increase in dopant density beyond the Mott critical concentration. This stands in stark contrast to the case of Mn-doped samples.

To further highlight the differences between magnetic and non-magnetic dopants in GaAs, we plot our results for the  $\text{Ga}_{1-x}\text{Mn}_x\text{As}$  samples, as well as the  $\text{Ga}_{0.991}\text{Be}_{0.009}\text{As}$  sample in Fig. 3a. Fig. 3b shows scaled conductivity for these samples, as well as earlier IR data for  $\text{Ga}_{1-x}\text{Mn}_x\text{As}$ , normalized by  $\sigma_1(\omega)$  at  $\omega_0$  along the  $y$ -axis, and by  $\omega_0$  along the  $x$ -axis. In both Mn- and Be-doped samples we observe a mid-IR resonance, however a result that stands out in both panels is the difference in lineshape of this resonance in genuinely metallic  $\text{Ga}_{1-x}\text{Be}_x\text{As}$  and that in the Mn-doped samples. The resonance seen in  $\text{Ga}_{0.991}\text{Be}_{0.009}\text{As}$  is much narrower and reveals a two-peak structure. The second peak appears as a shoulder on the main peak, and is most clearly seen near  $\omega/\omega_0=1.5$  in Fig. 3b. The frequency position of the two-peak structure is an order of magnitude higher than  $E_{\text{Be}}$ , however it is near the energy expected for intra-VB transitions, in accord with  $E_F$  located deep within the VB. The main peak is thus attributed light-hole band (LH) to heavy-hole band (HH) excitations [25], while the shoulder is due to excitations from the split-off band (SO)[26].

In contrast to our observations in the  $\text{Ga}_{0.991}\text{Be}_{0.009}\text{As}$  film, all the Mn-doped samples (both in the insulating regime and those past the onset of conductivity) show very broad, structureless absorption. Furthermore, upon scaling of

these data (Fig. 3b), the Mn-doped samples reveal a nearly identical lineshape, barring small non-monotonic differences in the width mid-IR peak resonance. The similar lineshape is indicative of a similar origin of the mid-IR resonance in both insulating and conducting samples (VB to IB optical excitations). The scaled  $\text{Ga}_{1-x}\text{Mn}_x\text{As}$  data include early IR results, with different growth procedures (rotated and non-rotated, post growth annealing, etc.) that imply variable levels of disorder, yet the qualitative features reveal only minimal dependence on the degree of disorder. These facts allow us to conclude that disorder is not playing a major role in the infrared response of  $\text{Ga}_{1-x}\text{Mn}_x\text{As}$ . Another result evident from Fig. 3 is the prominent Drude peak observed only in  $\text{Ga}_{1-x}\text{Be}_x\text{As}$  samples. Much weaker low-energy spectral weight is exhibited in Mn-doped samples, even those subjected to low-temperature annealing known to enhance the carrier density[30] (further discussion of low- $\omega$  analysis of Be and Mn-doped samples can be found in supplemental materials). All these findings demonstrate the distinct nature of transport in films with magnetic Mn-dopants.

Simple models, such as that calculated according to the quantum defect method for band-to-acceptor transitions (black dashed Fig. 3) [12] (see supplementary material for model details), as well as more complex calculations [27, 28] been shown to successfully capture key aspects of the mid-IR resonance in  $\text{Ga}_{1-x}\text{Mn}_x\text{As}$ . However, other explanations of the mid-IR resonance have been proposed [8], and the microscopic justification of such “impurity band models” have been called into question [29]. Our systematic study showing the mid-IR resonance exists in the insulating regime, and persists with the same lineform across the IMT up to the highest attainable doping, conclusively demonstrates impurity states dominate electronic dynamics in  $\text{Ga}_{1-x}\text{Mn}_x\text{As}$ , even in highly conductive samples.

Aspects of coexistence of the IB and metallicity are perhaps understandable very near the IMT, as in the case of the  $x=9.5\times 10^{-5}$  Be-doped sample. However our results show that in the magnetically doped films, signatures of IB states remain, along with the co-existence of metallic and insulating trends, at least an order of magnitude in dopant concentration beyond that associated with the onset of conduction. Theoretical work has directly linked exchange coupling between Mn-ions and valence holes to the persistence of the IB in  $\text{Ga}_{1-x}\text{Mn}_x\text{As}$  [37, 38], further underscoring the pivotal role of magnetism in the electronic structure and optical phenomena of  $\text{Ga}_{1-x}\text{Mn}_x\text{As}$ . Because trivial clustering of multiple phases has been ruled out in  $\text{Ga}_{1-x}\text{Mn}_x\text{As}$  [31, 32], the duality between metallic and insulating trends appear to be an intrinsic attribute of the IMT in magnetically  $p$ -doped GaAs [33]. In view of the above duality, it may not be surprising that some properties of  $\text{Ga}_{1-x}\text{Mn}_x\text{As}$  can be explained from the standpoint of Bloch-like states [29, 34, 35]. However, many salient features of  $\text{Ga}_{1-x}\text{Mn}_x\text{As}$  cannot be understood in the context of conventional VB conduction, such as the spectral features and activated trends seen in Fig. 1, and require an emphasis

on localization [27, 28, 36]. We speculate electronic correlations are likely to be vitally important in a conducting system at the borderline of localization, and note earmarks of such electron-electron effects have been identified in  $\text{Ga}_{1-x}\text{Mn}_x\text{As}$  tunneling spectra [32]. Though disorder plays a role, our experiments show that disorder alone is not sufficient to explain the radical differences between Be-doped and Mn-doped samples.

Work at UCSD is supported by the Office of Naval Research. Work at UCSB is supported by the Office of Naval Research and the National Science Foundation.

## I. SUPPLEMENTARY MATERIAL

### A. Materials and Methods

All films in this study were prepared at UCSB using molecular-beam-epitaxial (MBE) growth, on insulating (001) GaAs substrates. Since this study involved several doping regimes, some of the details of the growth vary between samples. All of the  $\text{Ga}_{1-x}\text{Mn}_x\text{As}$  films studied were prepared following the non-rotated, low-temperature growth techniques reported in Ref.[3, 4] (see IB). Specific details on growth properties of all samples can be found in Table II. The  $x=0.015$ , 0.03, and 0.092 samples were also subjected to low-temperature annealing, which has been shown to remove Mn-interstitials in  $\text{Ga}_{1-x}\text{Mn}_x\text{As}$ , increasing the carrier density  $p$  and  $T_C$ , as well as improving other sample properties [39]. Note the  $x=0.015$  and 0.015\*  $\text{Ga}_{1-x}\text{Mn}_x\text{As}$  films are the same sample pre- and post-annealing, as well as for the  $x=0.03$  and 0.03\*  $\text{Ga}_{1-x}\text{Mn}_x\text{As}$  films (\* indicates the sample was annealed).  $\text{Ga}_{1-x}\text{Mn}_x\text{As}$  samples of  $x=0.005$ , 0.0075 were found to be paramagnetic (PM) at all locations along the films. The other more heavily doped  $\text{Ga}_{1-x}\text{Mn}_x\text{As}$  films were found to be ferromagnetic (FM), with  $T_C$  in the region of minimized compensating defects listed in Table II. In the  $x=0.015^*$  and 0.03\*  $\text{Ga}_{1-x}\text{Mn}_x\text{As}$  samples,  $T_C$  after annealing was determined by the temperature of maximum low-frequency resistivity ( $\rho_{\text{IR}}=1/\sigma_1(40 \text{ cm}^{-1})$ ). For all other samples, including  $x=0.015$  and  $x=0.03$  before annealing,  $T_C$  was measured in a SQUID magnetometer. The  $\text{Ga}_{0.991}\text{Be}_{0.009}\text{As}$  was grown to a nominal thickness of  $t=100$  nm, also using the non-rotated, low-temperature technique at 250 °C. The  $\text{Ga}_{1-x}\text{Be}_x\text{As}$  samples of  $x=3.8\times 10^{-5}$ ,  $9.5\times 10^{-5}$ , and  $3.2\times 10^{-4}$  do not require low-temperature conditions during growth because of their relatively low doping concentrations. The Mn dopant concentration was determined by growth rate calibrations of MnAs and GaAs RHEED oscillations, while the concentration in Be-doped samples was determined from room temperature Hall-effect measurements. Deviations between  $p$  extracted from Hall measurements and actual Be concentration are expected to be minor due to the small, and in some cases non-existent, activation energy in the



dopant	concentration (%)	nominal thickness (nm)	growth temperature ( $^{\circ}\text{C}$ )	annealing temperature ( $^{\circ}\text{C}$ )	$T_C$ (K)
Mn	0.5	200	250	-	< 4
	0.75	200	250	-	< 4
	1.5	200	250	-	21
	1.5*	200	250	220	21
	3.0	200	220	-	42
	3.0*	200	220	200	60
	9.2*	100	200	180	130
	16	100	150	-	120
Be	0.0038	980	580	-	-
	0.0095	980	580	-	-
	0.032	980	580	-	-
	0.9	100	250	-	-

TABLE II: Sample growth properties.

Be-doped samples.

All data presented in the manuscript on films grown the non-rotated technique were collected from  $d \sim 0.5$  mm spot where As-flux is tuned to maximize  $p$ . We therefore conclude that at this special location, compensation is minimized, as is disorder in general. This conjecture is supported through detailed transport studies of films prepared using similar growth protocol [3, 4]. For each sample, this particular location was established through systematic studies of IR spectra along the wafer, and determined by the location of the largest integrated spectral weight (see I C). Furthermore, room temperature transport measurements have confirmed that the location of maximum  $p$  corresponds also to the minimum resistivity, highest mobility, and in the case of FM samples, maximum  $T_C$  [3, 4].

### B. Non-rotated growth

Several films in the study ( $\text{Ga}_{1-x}\text{Mn}_x\text{As}$ :  $x=0.005, 0.0075, 0.0115, 0.03, 0.09, \text{ and } 0.16$ ;  $\text{Ga}_{1-x}\text{Be}_x\text{As}$ :  $x=0.009$ ) were prepared using the non-rotated, low-temperature, MBE growth techniques reported in Ref. [3, 4]. The low growth temperatures are required to suppress precipitation of secondary crystal phases, such as MnAs. However, the low growth temperatures also result in the formation of compensating defects. Of these defects, As-antisites ( $\text{As}_{\text{Ga}}$ ) are particularly problematic in that they are known to be double-donors (compensating two holes)[40], can reach

concentrations on the order of  $10^{20} \text{ cm}^{-3}$  ( $\sim 1\%$  of Ga sites)[41], and cannot be annealed out. The non-rotated growth method is a novel technique that systematically reduces the presence of  $\text{As}_{\text{Ga}}$ .

The non-rotated growth utilizes a geometry in which the MBE system provides a continuous variation in the As:Ga ratio across the wafer. Control of the  $\text{As}_{\text{Ga}}$  content is achieved by the precise tuning of the As-flux, via the As:Ga gradient. Studies along the As:Ga gradient reveal an optimized location along the wafer where  $\text{As}_{\text{Ga}}$  has been minimized. This optimized location has been shown to correspond to maximum hole density  $p$ , maximum mobility, and minimum resistivity[3]. In ferromagnetic samples, the optimized location also reveals maximized  $T_C$  for given Mn concentrations, as well as improved magnetization, and magnetic hysteresis curves[3, 4].

### C. Optical characterization

The non-rotated technique provides a continuously varying As:Ga growth ratio, and thus yields a film with a gradient density of compensating As-antisite defects across the wafer. Local transport and local optical measurements in principle enable studies of  $p$ -doped GaAs at the location where the density of these defects is minimized. In order to characterize the films in this study, extensive infrared (IR) spectroscopic measurements were done along the As:Ga gradient in samples grown using the non-rotated technique. The location of maximum  $p$  can be determined directly from transmission measurements, as maximum  $p$  corresponds to the maximum absorption. For this purpose we developed a broad-band (far-IR to near-ultraviolet) microscope compatible with the low-temperature (20 K) operation. The spatial resolution of the apparatus is below 1 mm which is appropriate for the series of films we investigated here. This assertion was validated through direct IR microscopy experiments with spatial resolution less than  $100 \mu\text{m}$ .

### D. Extraction of optical conductivity

Transmission spectra are dependent on both components of the complex conductivity spectra  $\sigma(\omega) = \sigma_1(\omega) + i\sigma_2(\omega)$ . Importantly, these two components are not independent, but linked through the Kramers-Kronig (KK) relations [42]. Adding complexity, in multi-layer samples the data will include contributions to the optical response from all layers. A convenient method for overcoming the complications of multi-layer systems, and extracting  $\sigma(\omega)$  for a single layer in a multi-layer sample, is via multi-oscillator modeling. In the case of the film/substrate system studied here, the substrate  $\sigma(\omega)$  is initially characterized, thus only  $\sigma(\omega)$  of the film must be extracted. The film layer is modeled using

multiple oscillators, all chosen to ensure Kramers-Kronig consistency.

Modelling of transmission data results in a KK consistent extraction of  $\sigma(\omega)$ , which reproduces the experimental data. However,  $\sigma_2(\omega)$  in an intra-gap region is mainly determined by processes above the band gap. Therefore, accurate determination of the intra-gap  $\sigma(\omega)$  must include experimental input from at frequencies above the gap. In the case of GaAs substrates, the samples become opaque at frequencies above the GaAs band gap ( $\sim 12,000 \text{ cm}^{-1}$ ), placing a firm upper limit on the transmission data range. Thus, several films ( $x=0.005, 0.0075, 0.015, 0.03, 0.16 \text{ Mn}$  and  $x=0.009 \text{ Be}$ ) were also measured at room temperature using micro-ellipsometry for  $6,000 \text{ cm}^{-1} \leq \omega \leq 40,000 \text{ cm}^{-1}$ , with spatial resolution  $d \sim 150 \text{ }\mu\text{m}$ . Ellipsometry measures the ratio of the complex reflectivity coefficient ( $r$ ) of  $s$ - and  $p$ -polarized light. The experimental observables are the ellipsometric angles  $\psi$  and  $\Delta$  according to,

$$\frac{r_p}{r_s} = \tan(\psi)e^{i\Delta}, \quad (2)$$

where the subscript denotes the incident polarization. Ellipsometry data also have the additional advantage that they contain both magnitude and phase information. Thus, both components of  $\sigma(\omega)$  can be directly and uniquely extracted from the data over the entire ellipsometric frequency range via multi-oscillator modelling. One is therefore able, by simultaneous fitting of the model to the ellipsometry and transmission data, to produce KK consistent extraction of  $\sigma(\omega)$  over entire experimental range, with a high degree of confidence in the uniqueness and accuracy. Fig. 4 displays representative plots illustrating the  $\sigma(\omega)$  extraction procedure, showing experimental data and model fit, as well as the resulting  $\sigma(\omega)$  for the  $\text{Ga}_{0.985}\text{Mn}_{0.015}\text{As}$  sample. Fig. 5 shows the experimental transmission data and model fits of the  $x=3.8 \times 10^{-5}$ ,  $9.5 \times 10^{-5}$ , and  $3.2 \times 10^{-4}$  samples, along with the  $\sigma_1(\omega)$  curves for the corresponding models.

### E. Quantum Defect Model

The mid-IR resonance observed in the  $\text{Ga}_{1-x}\text{Mn}_x\text{As}$  was modeled using the quantum defect method [43]. This model was first applied to absorption in semiconductors by Bebb *et al.* [44], and later used to model absorption in magnetic semiconductors such as  $\text{Cd}_{1-x}\text{Mn}_x\text{Te}$  [45] and  $\text{Ga}_{1-x}\text{Mn}_x\text{As}$  [12]. In this model, the cross section for photoionization transitions associated with a given band is written as,

$$S(\hbar\omega) = \frac{4\pi\alpha_0}{3n(\hbar\omega)} \left[\frac{m^*}{m_0}\right]^2 \left[\frac{E_{\text{eff}}}{E_0}\right]^2 \frac{2^{2\nu}(\nu\alpha^*)^2 f(y)}{y^{1/2}(1+y)^\nu},$$

$$f(y) = \left[ \frac{\sin[(\nu+1)\tan^{-1}(y^{1/2})]}{y^{1/2}} - \frac{(\nu+1)\cos[(\nu+2)\tan^{-1}(y^{-1/2})]}{(1+y)^{1/2}} \right]^2, \quad (3)$$

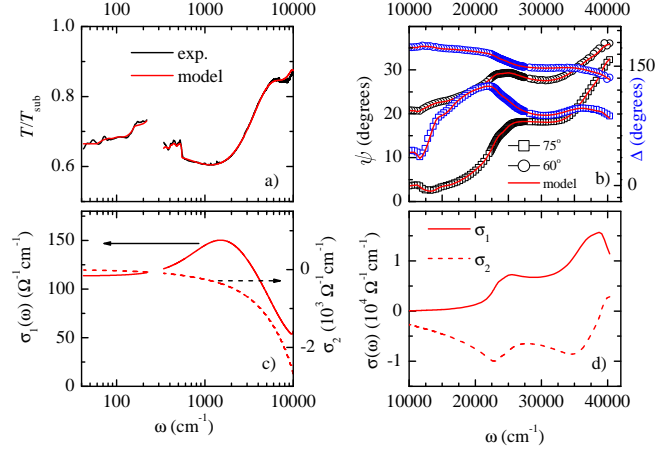


FIG. 4: Representative room-temperature transmission and ellipsometry data is shown with model fit to highlight  $\sigma(\omega)$  extraction technique. All panels show data corresponding to the  $\text{Ga}_{0.985}\text{Mn}_{0.015}\text{As}$  sample. a) Experimental transmission spectrum normalized by transmission of the substrate, along with the multi-oscillator model fit. b) Ellipsometric angles  $\psi$  and  $\Delta$  (see Eq. 2) measured at  $75^\circ$  and  $60^\circ$  angle of incidence is shown with the model fit. (c and d) Real ( $\sigma_1(\omega)$ ) and imaginary ( $\sigma_2(\omega)$ ) components of the  $\sigma(\omega)$  spectrum resulting from the model are shown. Note red data in all four panels represent the same model, which provides a KK consistent fit of all experimental data across the entire frequency range.

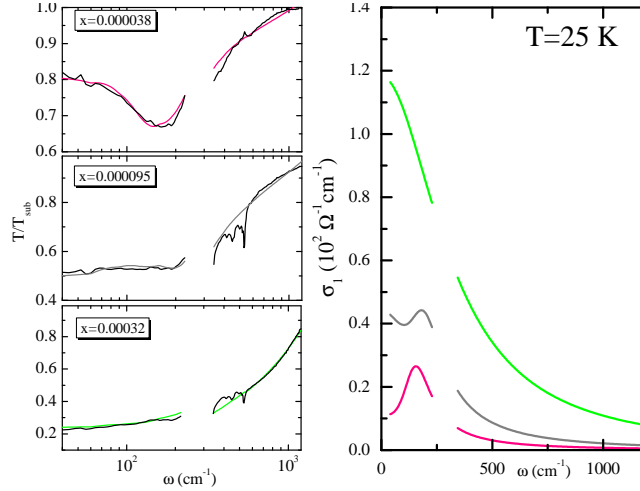


FIG. 5: (Left panels) Low temperature transmission of  $\text{Ga}_{1-x}\text{Be}_x\text{As}$  near the IMT normalized to the substrate transmission (black) along with model fits. (Right panel) Low temperature  $\sigma_1(\omega)$  spectra extracted from the transmission data.

$$y = \frac{\hbar\omega - E_i}{E_i},$$

where  $n(\hbar\omega)$  is the frequency dependent index of refraction,  $\alpha_0$  the fine structure constant,  $\nu = (R^*/E_i)^{1/2} = (e^4 m^*/2\hbar^2 \epsilon^2 E_i)^{1/2}$ , with  $E_i$  the Mn acceptor level,  $m^*/m_0$  the effective mass ratio determined

from the effective Bohr radius  $a^* = \hbar^2 \epsilon / m^* e^2$ , with  $\epsilon$  the static dielectric constant. Following Kojima *et al.* [12], the factor  $E_{\text{eff}}/E_0$  is set equal to 1.

In order to adapt this model to the case of  $\text{Ga}_{1-x}\text{Mn}_x\text{As}$ , and again following Kojima *et al.* [12], we add background and disorder effects. To take disorder into account we use a phenomenological Gaussian smearing with broadening factor  $\mu$ , resulting in the modified cross-section,

$$S_{BR}(\hbar\omega, E_i) = \frac{1}{\sqrt{2\pi\mu}} \int_{-\infty}^{\infty} e^{-(E'-E_i)^2/2\mu^2} S_{BR}(\hbar\omega, E') dE'. \quad (4)$$

The absorption spectrum is then given by,

$$\alpha(\hbar\omega, E_i) = N S_{BR}(\hbar\omega, E_i) + \alpha_B, \quad (5)$$

where  $\alpha_B$  is the background absorption assumed to be constant in this model, and  $N$  is the density of neutral Mn acceptors available to accept an electron from the VB to the Mn impurity level. Finally, the  $\sigma_1(\omega)$  spectrum is calculated by  $\sigma_1(\omega) = n(\hbar\omega) \alpha(\hbar\omega, E_i) / (4\pi \frac{1}{\lambda})$ . The curve shown in the manuscript uses  $\alpha_B = 14500 \text{ cm}^{-1}$ , an acceptor density of  $N = 10^{20} \text{ cm}^{-3}$ , and a broadening factor of  $\mu = 40 \text{ meV}$  taken from time-resolved spectrum in Ref. [12].

## F. low- $\omega$ analysis

An agreement is expected between the low- $\omega$   $\sigma_1(\omega)$  extracted from optics and dc values provided there are not other strong electronic excitations between  $40 \text{ cm}^{-1}$  and dc. While the gradient nature of the samples in this study complicates transport measurements, we note the dc conductivity for the  $\text{Ga}_{0.84}\text{Mn}_{0.16}\text{As}$  sample in this study are reported at the location of minimum compensation in Ref. [4], and show excellent agreement with the  $\sigma_1(40 \text{ cm}^{-1})$  value extracted from our optical probe.

Interestingly, the full-width at half-max of the Drude peak, quantifying the scattering rate within the Drude model, is not enhanced in the  $x=0.009$  Be-doped sample with respect to  $x=3.2 \times 10^{-4}$  Be-doped. Recalling that only the former was grown in low-temperature conditions points towards two possible scenarios: either the disorder in samples grown under low-temperature conditions is similar to lower-doped conventionally grown films; or the increase in disorder is effectively screened out by excess charges [8]. Note, neither of these scenarios is necessarily specific to the case of Be-doped GaAs. Furthermore, because  $m_{\text{opt}}$  is related to the band dispersion, the similar values found in the two metallic Be-doped samples suggests that whatever disorder is present, it is not significantly altering the

nature of states in the vicinity of the Fermi level ( $E_F$ ). Difficulties in accurately determining  $p$  in magnetic systems, and in decoupling delocalized Drude-like transport from interband transition contributions limit similar analysis of the scattering rate and  $m_{\text{opt}}$  in  $\text{Ga}_{1-x}\text{Mn}_x\text{As}$ . However, reasonable estimates reveal the effective mass of carriers in  $\text{Ga}_{1-x}\text{Mn}_x\text{As}$  to be significantly larger than that of the metallic Be-doped samples. Detailed quantitative analysis of  $\text{Ga}_{1-x}\text{Mn}_x\text{As}$  effective masses in IR data can be found in Ref. [10, 11].

- 
- [1] J. M. D. Coey et al., *Adv. Phys.* **48**, 167 (1999).
  - [2] K. Sato et al., *Rev. Mod. Phys.* **82**, 1633 (2010).
  - [3] R. C. Myers et al., *Phys. Rev. B* **74**, 155203 (2006).
  - [4] S. Mack et al., *Appl. Phys. Lett.* **92**, 192502 (2008).
  - [5] Y. Nagai and K. Nagasaka, *Infrared Phys. Techno.* **48**, 1 (2006).
  - [6] B. L. Sheu et al., *Phys. Rev. Lett.* **99**, 227205 (2007).
  - [7] R. Moriya and H. Munekata, *J. Appl. Phys.* **93**, 4603 (2003).
  - [8] T. Jungwirth et al., *Phys. Rev. B* **76**, 125206 (2007).
  - [9] J. Okabayashi et al., *Phys. Rev. B* **64**, 125304 (2001).
  - [10] E. J. Singley et al., *Phys. Rev. Lett.* **89**, 097203 (2002).
  - [11] K. S. Burch et al., *Phys. Rev. Lett.* **97**, 087208 (2006).
  - [12] E. Kojima et al., *Phys. Rev. B* **76**, 195323 (2007).
  - [13] K. Ando et al., *Phys. Rev. Lett.* **100**, 067204 (2008).
  - [14] S. Ohya et al., *Phys. Rev. Lett.* **104**, 167204 (2010).
  - [15] M. A. Mayer et al., *Phys. Rev. B* **81**, 045205 (2010).
  - [16] V. F. Sapega et al., *Phys. Rev. Lett.* **94**, 137401 (2005).
  - [17] L. P. Rokhinson et al., *Phys. Rev. B* **76**, 161201(R) (2007).
  - [18] Y. Okimoto et al., *Phys. Rev. Lett.* **75**, 109 (1995).
  - [19] K. Hirakawa, *Physica E* **10**, 215 (2001).
  - [20] D. N. Basov, *Rev. Mod. Phys.* **83**, 471 (2011).
  - [21] D. Romero et al., *Phys. Rev. B* **42**, 3179 (1990).
  - [22] A. Gaymann et al., *Phys. Rev. B* **52**, 16486 (1995).
  - [23] Choice in cut-off excludes contributions from excitations into the GaAs conduction band, and facilitates direct comparison with other studies in the literature [11, 23].
  - [24] J. Sinova et al., *Phys. Rev. B* **66**, 041202 (2002).

- [25] W. Songprakob et al., J. Appl. Phys. **91**, 171 (2002).
- [26] R. Braunstein and E. O. Kane, J. Phys. Chem. Solids **23**, 1423 (1962).
- [27] C. P. Moca et al., Phys. Rev. B **80**, 165202 (2009).
- [28] G. Bouzerar and R. Bouzerar, New J. Phys. **13**, 023002 (2011).
- [29] J. Mašek et al., Phys. Rev. Lett. **105**, 227202 (2010).
- [30] K. M. Yu et al., Phys. Rev. B **65**, 201303 (2002).
- [31] S. R. Dunsiger et al., Nature Mater. **9**, 299 (2010).
- [32] A. Richardella et al., Science **327**, 665 (2010).
- [33] V. F. Sapega et al., Phys. Rev. B **80**, 041202(R) (2009).
- [34] T. Jungwirth et al., Rev. Mod. Phys. **78**, 809 (2006).
- [35] T. Dietl et al., Science **287**, 1019 (2000).
- [36] R. Bouzerar and G. Bouzerar, EPL-Europhys. Lett. **92**, 47006 (2010).
- [37] A.-M. Nili et al., CondMat arXiv:1007.4609V1 (2010).
- [38] A. Chattopadhyay et al., Phys. Rev. Lett. **87**, 227202 (2001).
- [39] K. Edmonds, P. Boguslawski, K. Wang, R. Campion, S. Novikov, N. Farley, B. Gallagher, C. Foxon, M. Sawicki, T. Dietl, et al., Phys. Rev. Lett. **92**, 037201 (2004).
- [40] X. Liu, A. Prasad, J. Nishio, E. Weber, Z. Liliental-Weber, and W. Walukiewicz, Appl. Phys. Lett. **67**, 279 (1995).
- [41] M. Missous, J. Appl. Phys. **75**, 3396 (1994).
- [42] F. Wooten, *Optical Properties of Solids* (Academic, New York, London, 1972).
- [43] H. Bebb, J. Phys. Chem. Solids **28**, 2087 (1967).
- [44] H. Bebb, Phys. Rev. **185**, 1116 (1969).
- [45] C. Huber, J. Perez, and T. Huber, Phys. Rev. B **36**, 5933 (1987).